

Automatika

Journal for Control, Measurement, Electronics, Computing and Communications



ISSN: (Print) (Online) Journal homepage: www.tandfonline.com/journals/taut20

Early-stage breast cancer screening using a new biodegradable and easily implantable multi-element sensor in sub-THz range

Madan Kumar Sharma, Satyanarayana Degala & Abdullah Said Alkalbani

To cite this article: Madan Kumar Sharma, Satyanarayana Degala & Abdullah Said Alkalbani (2024) Early-stage breast cancer screening using a new biodegradable and easily implantable multi-element sensor in sub-THz range, *Automatika*, 65:4, 1677-1688, DOI: [10.1080/00051144.2024.2430505](https://doi.org/10.1080/00051144.2024.2430505)

To link to this article: <https://doi.org/10.1080/00051144.2024.2430505>



© 2024 The Author(s). Published by Informa UK Limited, trading as Taylor & Francis Group.



Published online: 24 Nov 2024.



Submit your article to this journal [↗](#)



Article views: 87




View related articles [↗](#)



View Crossmark data [↗](#)



Early-stage breast cancer screening using a new biodegradable and easily implantable multi-element sensor in sub-THz range

Madan Kumar Sharma , Satyanarayana Degala and Abdullah Said Alkalbani

Department of Computer Engineering, College of Engineering, University of Buraimi, Al Buraimi, Sultanate of Oman

ABSTRACT

In this article, a new biodegradable and easily implantable multi-element sensor is presented for early-stage breast cancer screening within the Sub-THz frequency range. The evolution of the sensor begins with the development of a single element. Once the desired operating frequency of operation is accomplished by the single element it is transformed into a multi-element configuration. The sensor is implemented on a compact size ($20,000 \times 20,000 \mu\text{m}^2$) easily biodegradable cordura substrate. The sensor performance is evaluated in terms of in-band reflection, directivity and surface current. The sensor is offered Fractional Bandwidth (FBW), average directivity and surface current density 115.15%, 10.5 dBi and 20 A/m, respectively. The breast phantom screening is carried out for normal and malignant phantoms of (Tis, N0, M0), (T1, N0, M0) and (T2, N1, M0) using the proposed Multi-Element Sensor (MES). The Principal Component Analysis (PCA) results, error bar and sensitivity parameters are accounted for in the analysis to discriminate the normal phantom from malignant phantoms. The sub-THz range of operation of the proposed sensor has opened a new research scope for medical screening applications and the proposed method comparatively, offers a wide range of measurements for tumour detection.

ARTICLE HISTORY

Received 20 March 2024
Accepted 12 November 2024

KEYWORDS

Breast cancer;
biodegradable; MES; PCA;
S-parameter

1. Introduction



Cancer is a leading cause of human mortality globally. As per recent global cancer patient statistics released by the International Agency for Research on Cancer (IARC), an estimated 19.23 million people were diagnosed with cancer, while 9.9 million lost their lives to the disease [1]. Among all types of cancer, breast cancer is a challenging disease for women's lives. As per the latest report of Globocan, about 2.3 million women have been diagnosed with breast cancer worldwide and 684,996 have lost their lives. As illustrated world mortality statistics in Figure 1 are due to all types of cancer detected among the women. The mortality percentage due to breast cancer is higher than that of other cancers.

Early warning signs of breast cancer, often detected by both patients and healthcare providers, include changes in breast shape, unexpected discharge, discomfort, nipple rash and swollen armpits. In some cases, lumps were also found in the breast. The study revealed that, aside from other symptoms, breast lumps were present in a subset of participants. Breast cancer primarily develops in the epithelial cells lining the ducts (85%) or lobules (15%) of the breast's glandular tissue [2]. Cancerous tissue initially grows around ducts or lobules. In the initial phase, no significant symptoms are observed and spreading rate is too slow [3]. Initially, cancerous cells spread surrounding breast tissue (invasive stage), subsequently, they may spread further to

regional lymph nodes (regional metastasis) or even distant organs in advanced cases [4]. Unfortunately, many women receive breast cancer diagnoses in stage 3 or 4. This delay often proves fatal as the cancer becomes difficult to treat. Early detection is crucial, as breast cancer's high mortality rate of 15% testifies [5]. Ignoring seemingly trivial symptoms can have dire consequences, so prompt medical attention and early diagnosis are key to reducing the risk of death.

Existing breast cancer detection methods like X-rays and mammograms pose radiation risks for younger women [6,7]. While MRI offers safer and more precise imaging, its cost and accessibility limitations leave a gap. Additionally, even advanced mammograms and MRIs struggle to pinpoint tiny, early-stage tumours (T1) in dense breast tissues [8]. Machine learning has played a pivotal role in enhancing the accuracy of medical imaging (X-ray, mammogram, MRI) through post-processing techniques, as explored in [9–11].

The potential of sub-THz microwave sensors for tumour detection has sparked intense scientific inquiry over existing modalities. In the sub-THz range (0.002–0.3 THz), these sensors offer superior signal penetration through human tissue [12], enabling better differentiation of small tumours from healthy tissues. Extensive research has yielded various microwave sensor designs for tumour detection in different organs, as detailed in references [13–18]. The authors in reference

CONTACT Madan Kumar Sharma  madansharma12@gmail.com, madan.k@uob.edu.om  Po. Box: 890, Pc: 512, Al Buraimi, Al Buraimi Governorate, Oman

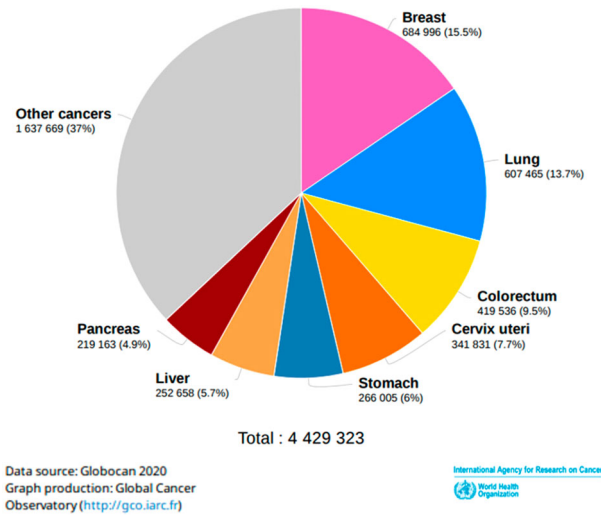


Figure 1. Estimated female mortality statistics worldwide due to all types of cancer [1].

[13] employed dielectric spectroscopy at 0.5–10 GHz using a Keysight probe and tissue phantoms to analyse the properties of skin and fat. To mimic breast tissue and detect tumours, an ex-vivo microwave imaging system, based on a double ridge waveguide sensor, has been implemented in [14]. This system uses a special signal processing technique to reconstruct images and successfully detect tumours based on their electrical properties. However, the diagnostic setup and microwave sensor were not conducive to ensuring patient comfort. The Vivaldi microwave antenna sensor, introduced in [15], underwent a simulation study in which a phantom model was employed for tumour detection. The sensor was constructed using a non-biodegradable material consisting of copper and dielectric, with dimensions of $73 \times 42 \text{ mm} \supset 2$. A novel convex optimization approach for focusing electrical fields at 30 GHz was showcased in [16]. This innovative technique enabled deeper penetration of EM waves into breast tissue, making it valuable for accurate scans of dense breast tissue. However, the study utilized a rectangular phantom, potentially causing discrepancies between the measured field strength and that of a more realistic, anatomically shaped breast phantom. The microwave sensor was developed on the Roger non-disposable and non-biodegradable substrate size of $130 \text{ mm} \times 130 \text{ mm}$. The ring resonator array developed in [17] presented a captivating approach for non-invasive breast tumour detection using metamaterials.

Further optimization is necessary to streamline the implementation, enhance patient comfort and explore the possibility of disposable substrates for a more user-friendly experience. Several recent studies [18–21] tried to match these specific requirements. In [18] presents a high-frequency microwave breast imaging system (16–20 GHz) operating on a rectangular phantom ($178 \times 50 \times 36 \text{ mm}$) made from a non-disposable hard Roger substrate. Tumour detection

relies on backscattered signal analysis via the root mean square method. While the reported method successfully locates tumours, its validity in realistic scenarios with complex tissue properties needs further validation. Researchers in [19,20] developed a non-disposable UWB-MIMO antenna sensor and tested its performance on three realistic breast phantoms: normal, single tumour and multiple tumours. In [21], a flexible non-disposable sensor is even tested on an actual human subject. Although the sensor is reusable, patients use the same undergarment during testing, raising hygiene concerns. A THz sensor using a tree-slotted metamaterial was developed by G. Rajalakshmi et al. [22] for detecting 25-mm tumours. The sensor resonated at 2.04 THz frequency but, it was implemented on the non-biodegradable substrate. A graphene-based circular ring resonator THz sensor has been developed for cancer screening in [23]. Graphene is also a biocompatible material but not biodegradable and this study only analysed reflection results on the interaction of cancerous cells with sensors. Kritika Singh et al. developed a rectangular patch of gold, and an array of Split Ring Resonator (SRR) etched in the ground plane [24]. The cancerous sample was placed between two antennas for measurement. The reported method has two limitations: firstly, it utilizes expensive metal i.e. gold and is fabricated on a non-biodegradable substrate.

Current breast cancer detection methods often use reusable sensors, raising hygiene concerns. Despite the flexibility and biocompatibility of sensors reported in [17,18], the intricate evaluation process of sensors has limited their practical application. Additionally, most existing sensors operate at GHz frequencies, limiting their ability to distinguish between healthy and cancerous tissues. This study introduces a new, disposable sub-THz sensor specifically designed for breast cancer detection. Sub-THz waves offer better tissue penetration and contrast than GHz frequencies, leading to more accurate detection of malignant tumours.

This work is contributed in terms of the following major points:

- (1) Propose a new, low-cost, disposable (single use), easily implantable and (biodegradable) environment-friendly multi-element THz sensor.
- (2) To test and analyse the sensor behaviour in the sub-THz operating frequency range and finalize the most suitable biodegradable substrate for the sensor development.
- (3) To test the sensitivity and accuracy of the sensor by the placement of it over healthy and malignant breast phantoms in different measurement scenarios.

Reminder of the article is organized in the following sections: Section 2 includes sensor development methodology and substrate selection analysis, sensor

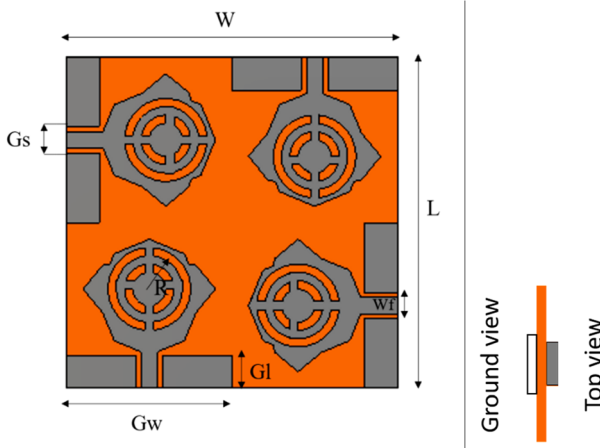


Figure 2. Design configuration of the proposed multi-element sensor, $L = 20,000 \mu\text{m}$, $W = 20,000 \mu\text{m}$, $G_w = 10,000 \mu\text{m}$, $G_s = 1500 \mu\text{m}$, $G_1 = 2000 \mu\text{m}$, $W_f = 1000 \mu\text{m}$, $R = 2000 \mu\text{m}$.

performance is evaluated in Section 3 and Phantoms design and modelling are defined in Section 4. The phantom analysis using sensors for tumour identification is described in Section 5, and finally work is concluded in Section 6.

2. Sensor development methodology

The proposed sensor is developed. In the first step, a single element is developed to accomplish the desired frequency band of sub-THz band. Furthermore, the single elements are orthogonally arranged on the Cordura flexible substrate with a dielectric constant of 1.1, a thickness of 1 mm and a loss tangent of 0.0098. The proposed multi-element sensor design configuration is depicted in Figure 2. A detailed discussion about sensor development is further explained in the next section.

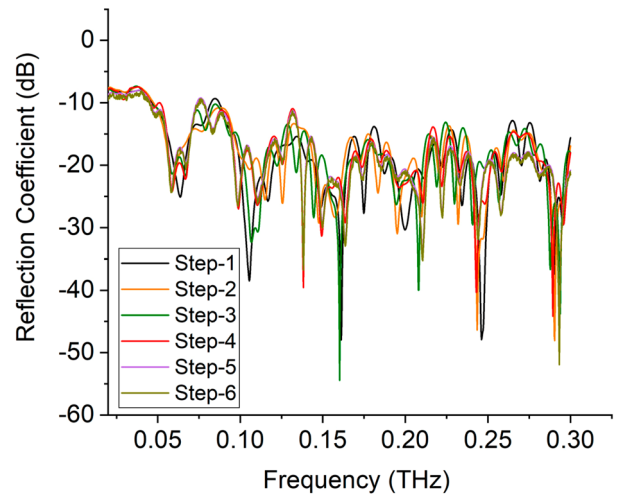


Figure 4. The reflection coefficient results from the stepwise evolution of the single element.

2.1. Single-element evolution of the sensor

The evolution process of the single element begins with an octagon-shaped patch created on the small size ($10,000 \times 10,000 \mu\text{m}^2$) Roger 5880 substrate with a dielectric constant of 2.2 and a loss tangent of 0.0009. A partial ground plane is also created on the top of the substrate along with the patch. Six design steps are followed to achieve the desired operating bandwidth (sub-THz range) of the single element. The stepwise development of the sensor element is shown in Figure 3. In the second step, another octagon-shaped structure is overlapped on the previous patch and the operating bandwidth results of each step are monitored and shown in Figure 4.

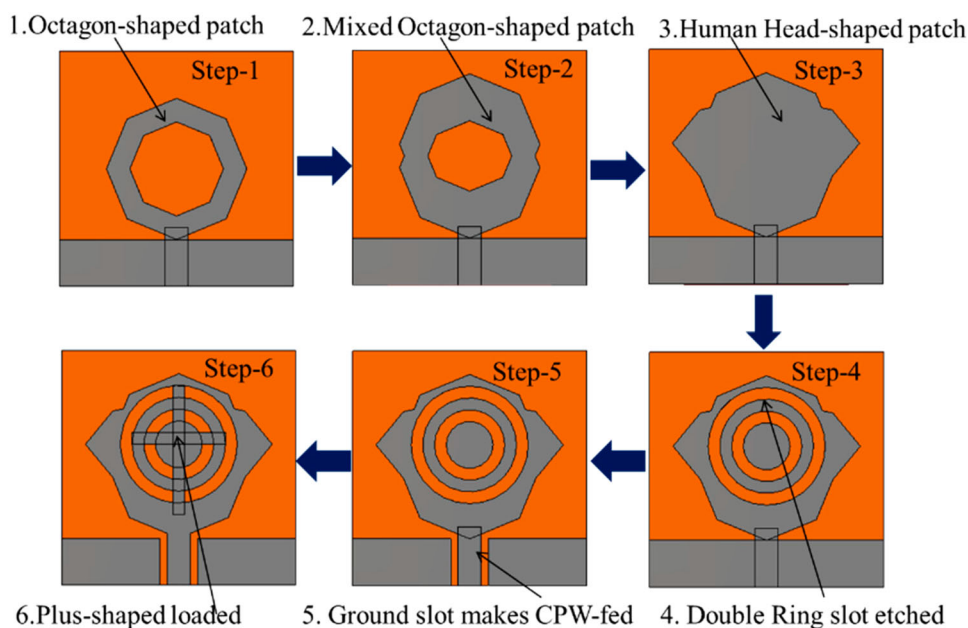


Figure 3. Step-wise development of a single element of the sensor.

2.2. Substrate selection and analysis

The flexible and comfortable substrate with better biodegradable disposability is an essential criterion of the proposed sensor development. The performance characteristics of the sensor are substantially depending upon the permittivity and thickness of the substrate [25]. Better performance can be accomplished with low relative permittivity, low dielectric loss and high thermal conductivity at the cost of increased overall size of the sensor. Therefore, miniaturization of the sensor without compromising their performance is also a considerable design challenge for researchers and Radio Frequency (RF) Engineers.

Given the above-discussed design constraint, four types of substrate included in the analysis i.e. Cotton, Jeans, Paper and Cordura with a permittivity of 1.6, 1.5, 2.3 and 1.1, respectively. The multi-element proposed sensor is designed on these selected substrates in the Computer Simulation Technology (CST) microwave studio design environment. The reflection coefficients and gain performance of the sensor with various substrates are analysed, as shown in Figure 5.

The reflection coefficient results of the proposed sensor with different substrates and selected a constant thickness of 1.5 mm. The calculated results as shown in Figure 5(a), a sensor with the jeans and the cotton substrate has in-band reflection ($S_{11} < -10$ dB) for the frequency range of 0.066–0.24 THz. The paper substrate is offered in-band reflection ($S_{11} < -10$ dB) for the frequency range of 0.05–0.23 THz. However, the sensor designed on the Cordura substrate offers the best operating bandwidth among all other substrates with in-band reflection ($S_{11} < -10$ dB) for the frequency 0.0074–0.265 THz. Undoubtedly, the operating bandwidth of the sensor with Cordura is better than that of the other substrates, but sensor performance is also analysed in terms of their gain to select the perfect

substrate. As shown in Figure 5(b), the gain of the sensor with jeans and the paper substrate is approximately the same and it is more than 10 dBi for the frequency 0.03–0.3 THz. The cotton substrate is offered a gain of 10 dBi for the range of 0.06–0.3 THz. However, the gain of the Cordura substrate is less than 10 dBi for the 0.03–0.2 THz frequency range and for the rest frequency range is more than 10 dBi. Although the gain for jeans and the paper substrate is relatively higher than for the Cordura substrate, operating bandwidth of jeans and the paper substrate is limited to 0.066–0.24 THz and 0.05–0.23 THz, respectively. Therefore, the gain and operating bandwidth criteria of the Cordura substrate are the best choice among the other substrates.

The sensor performance is further determined by different thicknesses of the Cordura substrate, as shown in Figure 6. The reflection results indicated that the in-band reflection ($S_{11} < -10$ dB) performance of the sensor is appropriate with the 1.0 mm-thick substrate which is offered an operating frequency range of 0.007–0.26 THz.

3. Performance analysis of the proposed sensor

The performance of the proposed sensor is evaluated in terms of directivity, surface current and s-parameters. While the phantoms are exposed through the sensor, the radiation intensity is an important parameter which defines the signal penetration quality. The directivity of the sensor is defined as the radiation intensity in a certain direction. The directivity of the sensor is evaluated at 0.06 and 0.1 THz frequency across the excited port 1 and port 2. The 3D patterns of evaluated directivity for port 1 and port 2 are shown in Figure 7; however, due to the symmetrical configuration of the other ports, assumed to offer similar results. The directivity offered by port 1 and port 2 at 0.06 THz frequency is 11.6

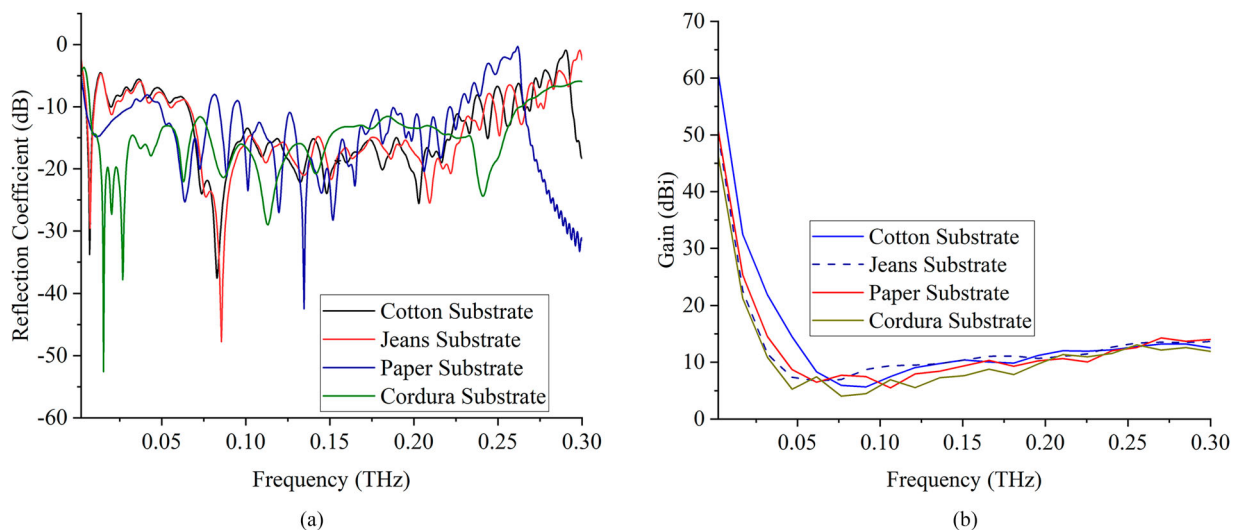


Figure 5. Substrate analysis results with different substrates, (a) Reflection Coefficient and (b) Gain.

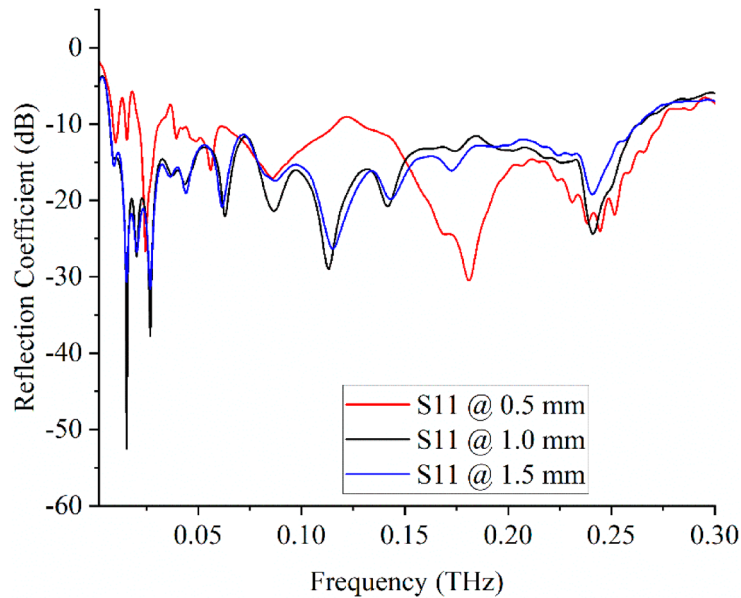


Figure 6. Reflection results of the sensor with different thicknesses of the substrate.

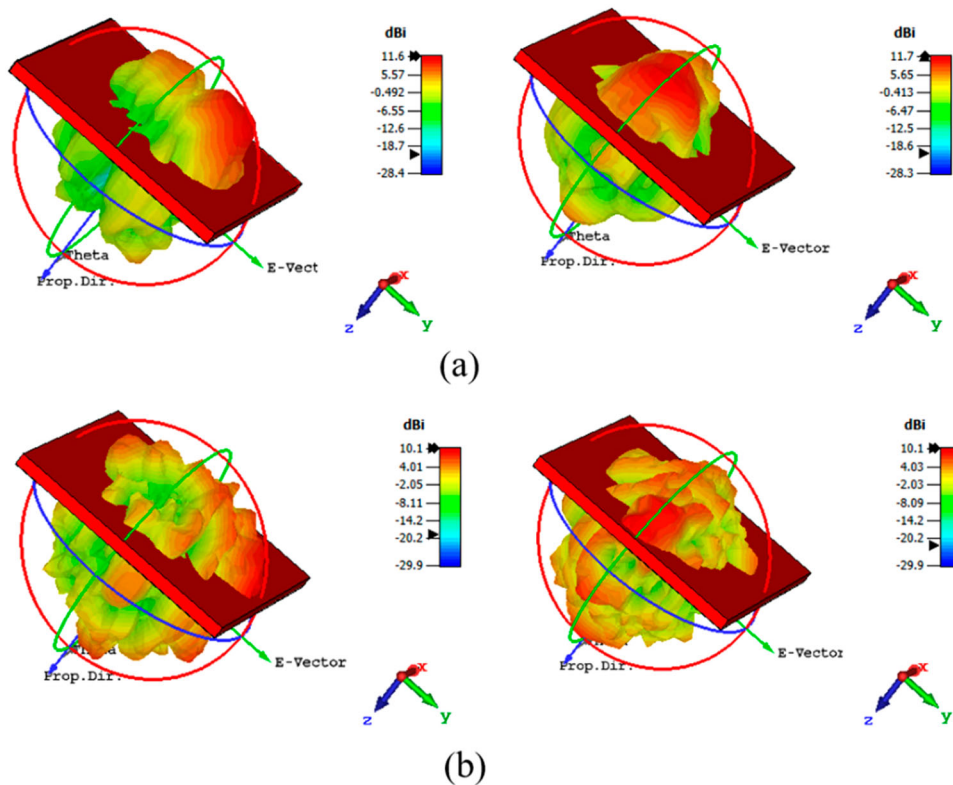


Figure 7. 3D Radiation pattern of the proposed sensor (a) at 0.06 THz, port 1 (left), port 2 (right) and (b) at 0.1 THz, port 1 (left), port 2 (right).

and 11.7 dBi, respectively. However, at the frequency 0.1 THz, both ports are offered the same directivity with the value of 10.1 dBi. Offered directivity by the proposed sensor has sufficient strength to penetrate in the breast phantoms.

The surface current distribution is another performance parameter of the sensor which is described as the port isolation among the sensing element. The evaluated surface current of the sensor is shown in Figure 8. The current density is observed across the non-excited

port and the amount of coupling is evaluated due to the induced current. The surface currents are monitored for port 1 and port 2 at 0.1 THz, 0.14 and 0.2 THz frequency, respectively, while one port is excited and the other terminated with a matched load of 50Ω . The results as monitored in Figure 8(a) with the port 1 excited and other remains non-excited, the maximum current density is observed around excited port 1; however, induced current across non-excited port is minimum. Similarly, Figure 8(b) with the port 2 excited

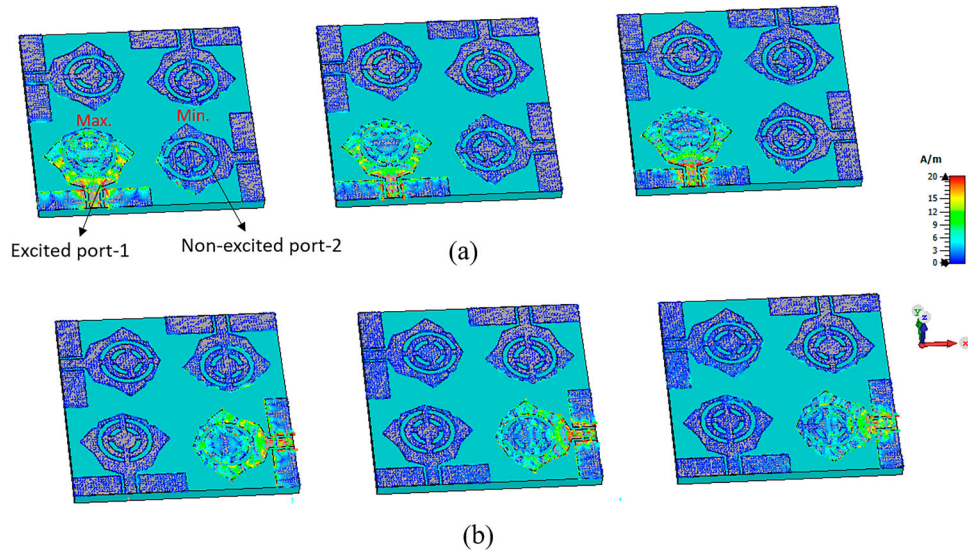


Figure 8. Surface current distribution across the sensor elements (a) at port 1 and (b) port 2 [The results monitored at 0.1 THz, 0.14 and 0.2 THz start in each row from left to right].

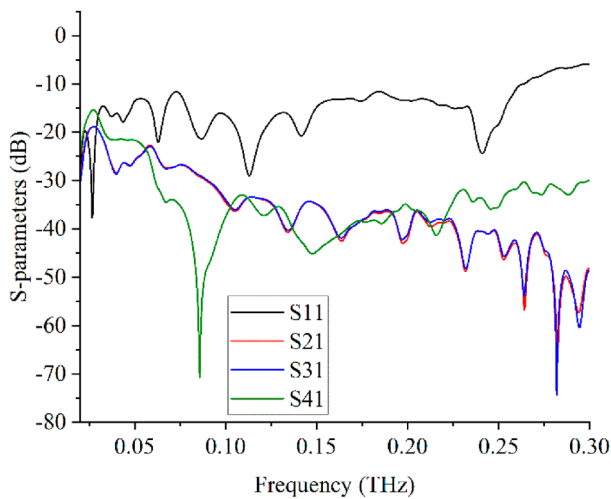


Figure 9. S-parameters of the proposed sensor.

and other remains terminated which also offered minimum current density. This self-isolated phenomenon of the sensor showed less coupling effect without introducing any decoupling mechanism resulting in the size miniaturization of the sensor.

S-parameters of the proposed sensor are depicted in Figure 9, the reflection result (S11) exhibits a wide operating bandwidth from 0.007 to 0.026 THz frequency. However, isolation parameters (S21, S31 and S41) exhibited port isolation of more than -30 dB for the desired operating frequency range. Although port isolation is a significant performance parameter in the communication systems, here we utilized this parameter as a phantom-sensing characteristic when the sensor interacted with different breast phantoms.

4. Phantoms design and modelling

According to the medical terminology, breast cancer is categorized and based on the (T, N and M) staging

systems. “T” stands for tumour size, “N” is the spreading stage around the lymph nodes and “M” is known as metastases, which refers to the spreading stage of the tumour in other body organs. Based on the (T, N and M) level cancers usually divide into Stage 0, Stage I, Stage II, Stage III and Stage IV [26]. Stage III and IV fall under the severe category in which clear evidence of the tumour can be easily assessed by conventional screening tools (X-ray, Mammogram and MRI). However, the assessment of the primary stages of the tumour is often difficult with these tools. Sometimes, dense breasts can not be examined through existing screening models, and need to pass through pathological examination through biopsy. However, biopsy is harmful and gives patients discomfort. Therefore, this study covers the primary stages of the tumour i.e. Stage 0 (Ductal carcinoma in situ), Stage I and Stage II. The categories of these models are described in [27] and defined in Table 1. The breast model with the cancerous tissue is shown in Figure 10.

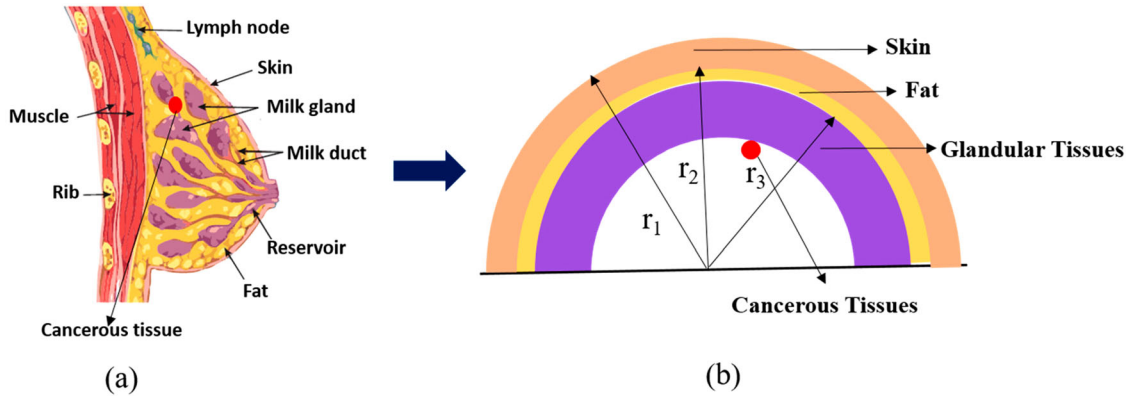
Based on the investigation criteria of tumour as summarized in the above table, a normal breast phantom model and three malignant phantom-layered models replicate in the bio-exposure environment of CST. The phantom model parameters are considered, as [29] described in Table 2. Once these models are prepared, further these models are evaluated using the proposed sensor for tumour analysis.

5. Tumour analysis using the proposed sensor

The tumour analysis is carried out using the proposed sensor, the sensor which is excited with ultra-impulse signal interacts in the near-field region with different breast phantom models, as described in section 4. The reflected and transmitted signals of the sensor exhibited a contrast due to different dielectric properties of

Table 1. Types of cancer asses in this study and their modelling.

Stage of cancer	Tumor size (mm)	Category	Spreading status
Stage-0	5	(Tis, N0, M0)	Present in the duct, symptoms are very low & non-invasive
Stage-I	15	(T1,N0,M0)	Small tumour, invasive & not spread to lymph nodes
Stage-II	35	(T2,N1,M0)	Tumour is spread in lymph nodes

**Figure 10.** Breast Models (a) Breast anatomy [28] and (b) Equivalent layered structure [19].**Table 2.** Phantom model parameters.

Breast layer	Radius of the layer (mm)	Relative permittivity (ϵ_r)	Relative conductivity (σ) (S/m)
Skin	$r_1 = 55$	36.5	4
Fat	$r_2 = 50$	10	0.4
Glandular tissue	$r_3 = 45$	10–16	0.5
Tumour	5, 15, 35	50.5	0.9

the phantom models over the frequency 0.002–0.3 THz. While the radiated signal from the sensor is incident on the phantom, the phantom has experienced two major electrical property changes, as described in [30] and permittivity (ϵ) changes are mentioned in Equation (1).

$$\epsilon = (\epsilon_s - j\epsilon_l) \quad (1)$$

where ϵ_s stored energy across the sample under test and ϵ_l imaginary part is known as energy losses across the sample and defined in Equation (2).

$$\epsilon_l = (\sigma / \omega \epsilon_0) \quad (2)$$

where (σ) is the conductivity, (ω) is known as the angular frequency and (ϵ_0) is a free space permittivity. The relative permittivity change is responsible for to change in sensor impedance and the cause of the deviation of reflection and transmission coefficient of the sensor. The evaluated reflection and transmission coefficient of the sensor without tumour and with tumour (5, 15, 35 mm) is shown in Figure 11. The minimum value of the reflection coefficient for normal phantom and malignant phantoms (5 mm tumour, 15 mm tumour and 35 mm tumour) are (−23.65) dB, (−20.65, −43.33, −39.75 dB), respectively. The difference in this value of reflection coefficient without tumour and (with 5 mm tumour, 15 mm tumour and 35 mm tumour) are 3, 19.68 and 16.1 dB, respectively.

The minimum value of transmission coefficient for normal and malignant phantoms (5, 15, 35 mm tumour) are −112 dB and (−64, −76.55, −72.65 dB), respectively. The difference between the normal and malignant phantom (5, 15, 35 mm tumour) transmission coefficient values are 48, 34.45 and 39.35 dB, respectively. These findings exhibited a sufficient contrast to separate healthy and malignant tissue of the breast.

5.1. Principal component analysis of S-parameters results

Even though the previous section carried out S-parameter analysis for normal and malignant breast phantoms to separate them from each other. But this evaluation process is limited by a single-valued function (Only considered minimum values of S-parameters for each case) out of 3001 observation points. Furthermore, Principal Components Analysis (PCA) is taken into account [31], which can include all observation points in tumour assessment and offers a more conclusive decision about breast tumour for each case. The PCA is a multivariate statistical tool to analyse a such large dataset of S-parameters effectively based on the correlation between the data points. The reflection and transmission coefficients for without tumour and with 5, 15 and 35 mm tumour are processed using PCA in XLSTAT (the trial version of the Microsoft Excel application). The PCA for reflection coefficient results is shown in Figure 12. The PC1 and PC2, the two main components, are used to explore how correlations change with and without tumour data for each case (5, 15 and 35 mm).

The correlation of principle components for without tumour and 5 mm tumour has PC1 and PC2 values of 69.51% and 30.49%, respectively. These components

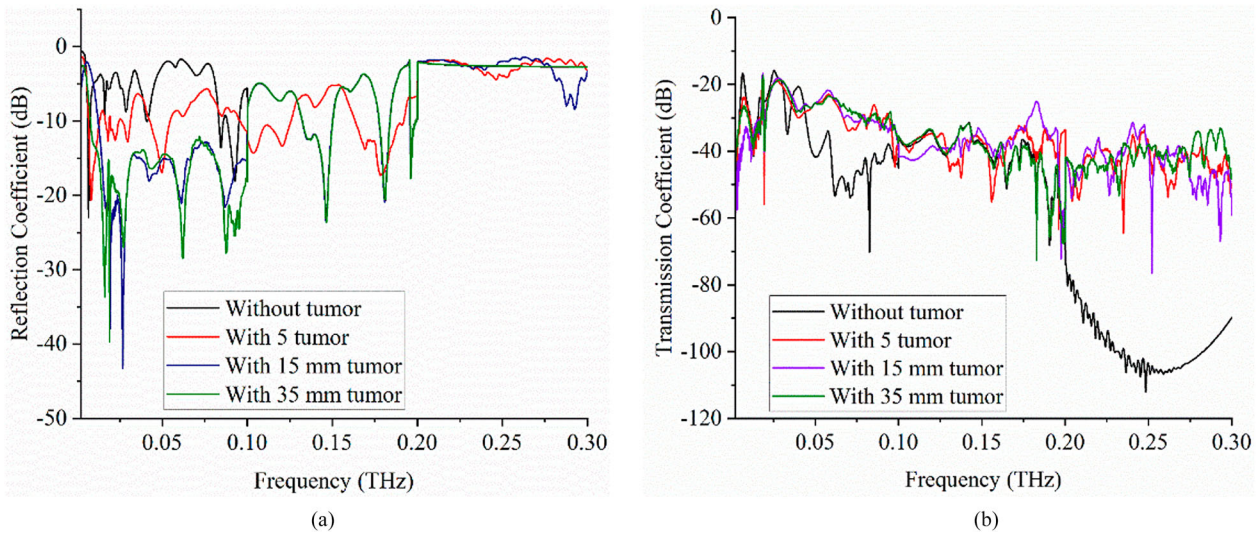


Figure 11. Tumour analysis on the interaction of the sensor with different phantoms (a) Reflection results and (b) Transmission results.

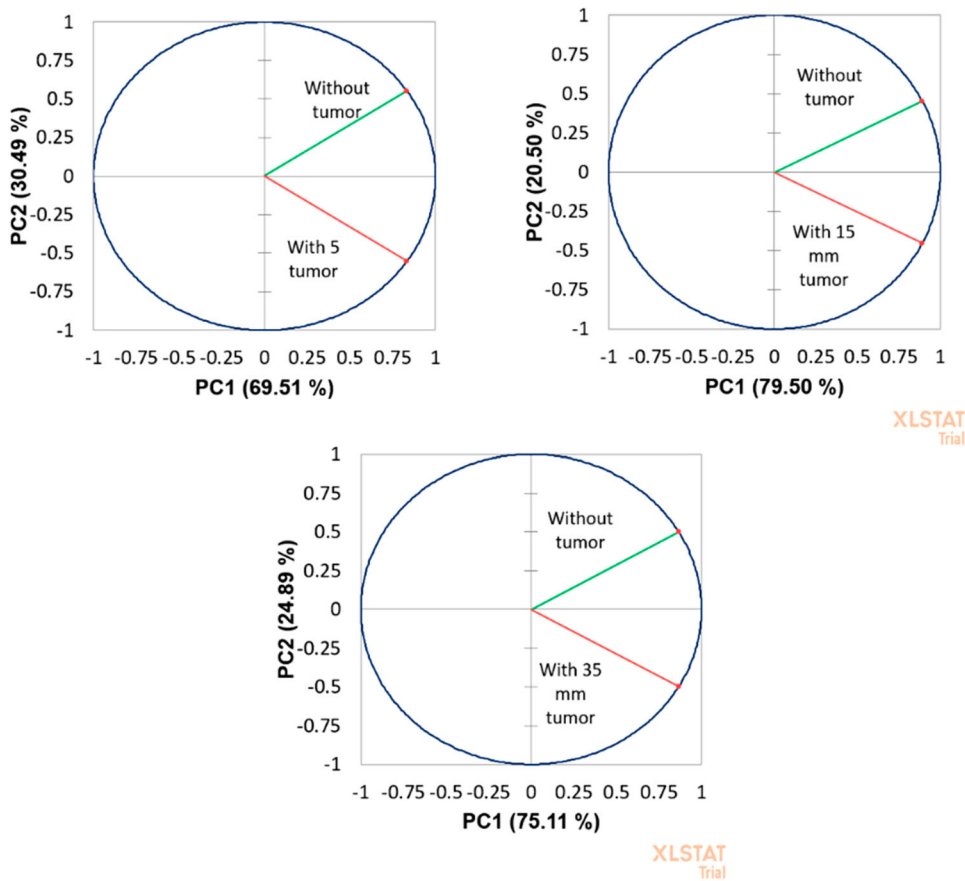


Figure 12. PCA results of reflection parameters [Analysis exhibits without tumour comparison with 5 mm tumour, 15 mm tumour and 35 mm tumour].

(PC1 and PC2) for 15 and 35 mm tumour cases are (79.5%, 20.5%) and (75.11%, 24.89%), respectively. The PCA components for the transmission coefficient are shown in Figure 13. The principal components (PC1 and PC2) for without tumour and 5 mm-tumour are (81.51% and 18.49%); however, these components for 15 and 35 mm tumour are (79.5% and 20.5%) and (75.11% and 24.89%), respectively.

From these results, we observed that for tumour cases, the principal components (PC1) are higher

than the principal component (PC2) for those without tumour cases.

5.2. Sensitivity analysis of the sensor

The sensitivity of the sensor was determined by calculating the statistical parameter (error bar) from the S-parameter results and considering the sensor’s resonating effects when interacting with normal and malignant phantoms containing tumours of varying sizes. These

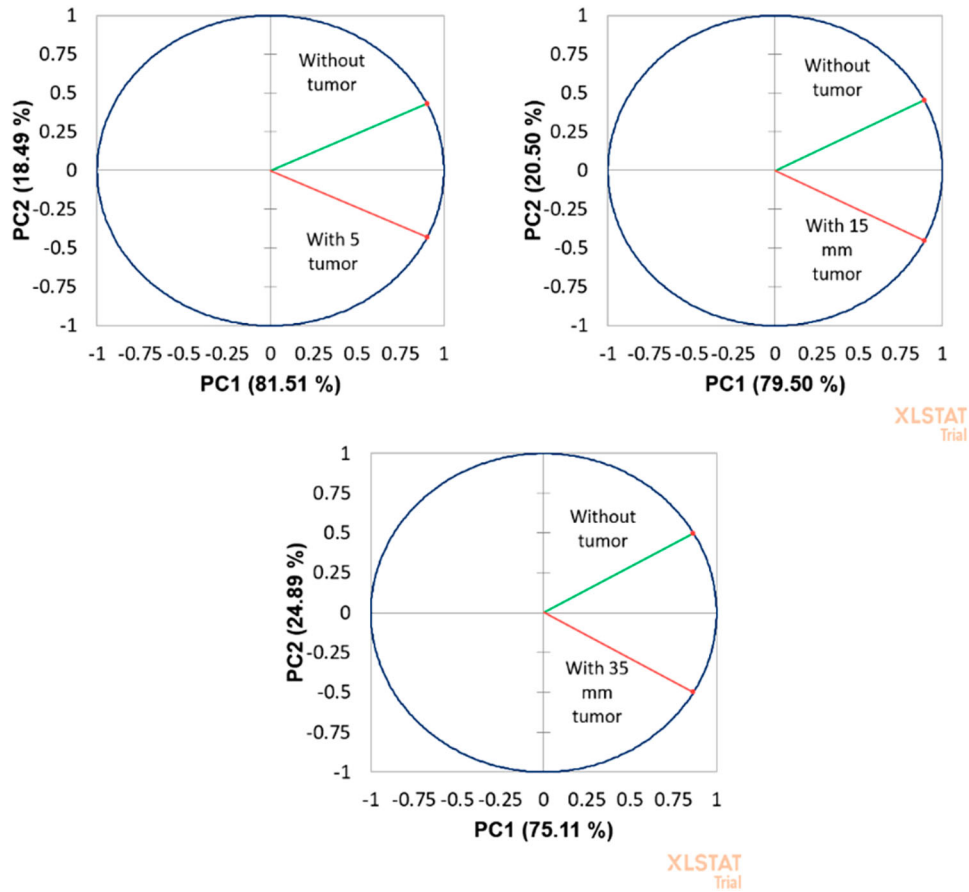


Figure 13. PCA results of transmission parameters [Analysis exhibits without tumour comparison with 5 mm tumour, 15 mm tumour and 35 mm tumour].

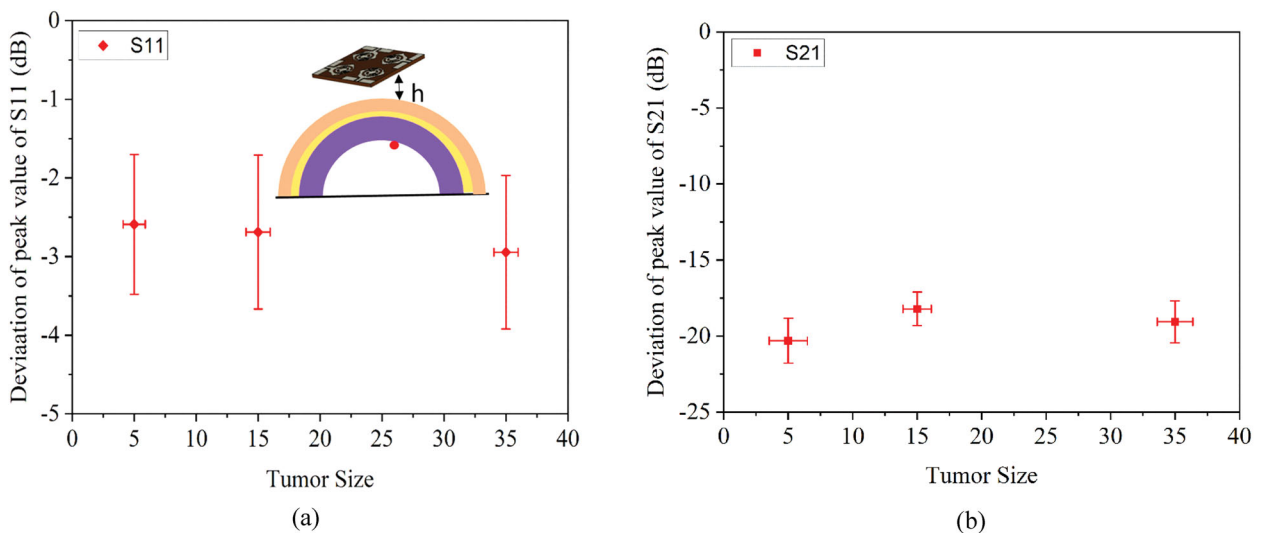


Figure 14. Error bar plots (a) for the peak value of reflection results and (b) for the peak value of transmission results.

analyses significantly confirmed the sensor's sensitivity. Each measurement is discussed in detail in the following sections.

The sensor is placed over malignant phantoms (with tumour size of 5, 15, 35 mm) in the near-field region at various heights ($h = 5, 15, 20$ and 25 mm), as

shown in Figure 14. For these four measurement trails, peak values of reflection and transmission results are observed and an error bar is drawn for both results. The error bar shows the deviation in the values for each case and the cause of the high sensitivity of the sensor.

Table 3. Sensitivity analysis of the sensor in different measurement scenarios.

SUT	(f_{r-max}) (GHz)	(f_{r-min}) (GHz)	Δf_r (GHz)	S21min (dB)	S21max (dB)	ΔS_{21} (dB)	Sensitivity (%)
Free space	282	28	254	-66.89	-18.86	48.03	19
Without tumour	240	25	215	-112	-15.8	96.2	45
5 mm tumour	235	26	209	-64.5	-18.55	45.95	22
15 mm tumour	252	19	233	-76.55	-16.74	59.81	26
35 mm tumour	183	19	164	-72.65	-17.21	55.44	34

Table 4. The computational complexity of the proposed experimental analysis, [Run on HP-made i-7 machine, with 16 GB RAM].

Simulation state of the sensor	Optimization environment of CST	Number of mesh cells	Maximum solver run	Total simulation Cost
Free space	Transient solver for planar device design	525,769	4054	4 h, 26 m, 5 s
Without tumour	Transient solver for biomedical exposure environment	985,953	6456	7 h, 34 m, 52 s
With tumour	Transient solver for biomedical exposure environment	995,789	6897	7 h, 54 m, 32 s

Sensor sensitivity is also evaluated by S-parameter results (S11 and S21) as described in [32] and defined by Equation (3). The sensitivity is evaluated for different cases (free space, without tumour, 5 mm tumour, 15 mm tumour, 35 mm tumour). The sensitivity results are summarized in Table 3.

$$S(\%) = \left(\frac{\Delta S_{21}}{\Delta f_r} \right) \times 100 \quad (3)$$

where (S) is the sensitivity, (ΔS_{21} = difference of $S_{21_{min}}$ and $S_{21_{max}}$) and (Δf_r) is the difference between relative resonate frequency for these (min) and (max) values.

Evaluated sensitivity for free space, without tumour, with 5 mm tumour, 15 mm tumour and 35 mm tumour is 19%, 45%, 22%, 26% and 34% respectively. In the CST simulation environment, the sensor placement over the breast phantoms was exact as described in the second paragraph of this section. However, a potential source of error may arise while these measurements are carried out in practical scenarios. In practice, to avoid such constraints, systems must develop with an adjustable sensor holder with a (mm) scale.

5.3. Computation complexity of the executed analysis

The computational complexity for simulations in the CST environment with body phantoms is heavily influenced by machine specifications, frequency of operation and the size of the chosen human body model. To achieve faster results, high-performance hardware is typically necessary. Table 4 provides a summary of the computational challenges encountered in this analysis.

5.4. Comparative study of the proposed sensor

A comparative analysis with existing work is discussed in terms of sensor disposability, operating frequency range, employed measurement techniques, assessment of tumour size, sensor type, sensitivity and sensor substrate used. Table 5 shows all the related details of

these parameters. Comparatively, the proposed multi-element sensor has a wider operating range than the sensors implemented in [13–18] and in [21,33] which can provide a broad range of dielectric characterization of the phantom models. However, measurement techniques of [16,21,33] can more effectively localize the tumour position.

In terms of assessing tumour size or stages, the claimed works in [13,15,17,18] assessed the single stage (i.e. stage-0) tumour; however, the proposed sensor assessed several early stages of the tumour (i.e. stage 0, stage 1 and stage 2). Works implemented in [21,33] utilized flexible and biocompatible substrates for sensor fabrication. In comparison, the proposed sensor substrate has biodegradability and flexibility, which is more environment-friendly and maintains patient hygiene by single-used property of the sensor. Overall, the sensitivity and assessment approach of the proposed sensor has wide applicability to early-stage breast cancer screening.

6. Conclusion

In this work, early-stage breast cancer screening has been successfully carried out using a new multi-element biodegradable sensor. The sensor performance is verified in terms of operating frequency range, gain, directivity and surface current distribution. The sensor offers a 0.007–0.26 THz operating frequency range, more than 10 dBi gain and good directivity and is most suitable for breast phantom evaluation. Three stages of the tumour (Stage 0 to Stage 3) are analysed using the proposed sensor. The reflection and transmission coefficient analysis are carried out and these results are well separate from the normal and malignant cases. Furthermore, a more accurate assessment of the tumour in each case is defined by the carried out PCA analysis. The proposed sensor sensitivity is evaluated by performing various experimental trials by changing the gap between the sensor and SUT in terms of error bar. The offered sensitivity for free space, without tumour, with 5 mm tumour, 15 mm tumour and 35 mm tumours is 19%, 45%, 22%, 26% and 34%, respectively. Comparatively,

Table 5. Comparison study of the proposed work with existing literature.

Ref.	Sensor type	Operating range (THz)	Tumor size assessed (mm)	Sensor substrate	Measurement techniques	Sensor disposability	Sensor sensitivity
[13]	Keysight made probe	0.0005–0.01	*	*	Permittivity analysis	No	Not defined
[14]	Double ridge waveguide	0.018–0.05	8	FR4	Inverse scattering	No	Not defined
[15]	Vivaldi antenna	0.005–0.01	5	FR4	CNR	No	Not defined
[16]	CP antenna	0.02–0.04	*	Rogers	Field focusing	No	Not defined
[17]	Antenna array	0.002–0.012	5	FR4	Inverse scattering	No	Not defined
[18]	Bowtie-like antenna	0.016–0.02	8	Rogers	RMSD	No	Not defined
[33]	Flexible antenna array	0.002–0.004	*	Kapton polyimide	SVM	No (Biocompatible)	Not defined
[21]	Flexible antenna array	0.002–0.004	*	Polyimide	DMAS	No	Not defined
This work	Multi-element	0.007–0.26	5, 15, 35 (Multi-stage)	Cordura (flexible)	Reflection, Transmission, PCA, error bar	Yes, (Biodegradable), single used	Defined For each case

the proposed sensor has low cost, biodegradability and multi-stage tumour assessment capability considered an alternative solution in breast cancer diagnosis. In this work, results are analysed by variation of distance between the sensor and SUT. For a more accurate diagnosis, the sensor should be rotated 360° over the breast along with distance. In future, a realistic setup can be designed which can scan the breast in a realistic environment using a proposed sensor.

Disclosure statement

No potential conflict of interest was reported by the author(s).

Funding

This research is carried out by the faculty of the College of Engineering at the University of Buraimi, Oman, under the Internal Research Grant Scheme of the University [grant number: IRG/UoB/CoE-002/2022-23].

ORCID

Madan Kumar Sharma  <http://orcid.org/0000-0002-3410-5594>

References

- [1] Cancer today. [cited 2023 Dec 22]. Available from: <https://gco.iarc.fr/today/home>
- [2] Makki J. Diversity of breast carcinoma: histological subtypes and clinical relevance. *Clin Med Insights Pathol.* 2015;8(1):23–31. doi:10.4137/cpath.s31563
- [3] Bish A, Ramirez A, Burgess C, et al. Understanding why women delay in seeking help for breast cancer symptoms. *J Psychosom Res.* 2005;58(4):321–326. doi:10.1016/j.jpsychores.2004.10.007
- [4] Singletary SE, Connolly JL. Breast cancer staging: working with the sixth edition of the AJCC cancer staging manual. *CA Cancer J Clin.* 2006;56(1):37–47. doi:10.3322/canjclin.56.1.37
- [5] Global cancer observatory. [cited 2023 Dec 22]. Available from: <https://gco.iarc.fr/>
- [6] Götzsche PC. Mammography screening is harmful and should be abandoned. *J R Soc Med.* 2015;108(9):341. doi:10.1177/0141076815602452
- [7] Grimm LJ, Avery CS, Hendrick E, et al. Benefits and risks of mammography screening in women ages 40 to 49 years. *J Prim Care Community Health.* 2022;13:1–6. doi:10.1177/21501327211058322
- [8] Gegios AR, Peterson MS, Fowler AM. Breast cancer screening and diagnosis: recent advances in imaging and current limitations. *PET Clin.* 2023;18(4):459–471. doi:10.1016/j.cpet.2023.04.003
- [9] Sahu A, Das PK, Meher S. An efficient deep learning scheme to detect breast cancer using mammogram and ultrasound breast images. *Biomed Signal Process Control.* 2024;87:105377. doi:10.1016/j.bspc.2023.105377
- [10] Sahu A, Das PK, Meher S. Recent advancements in machine learning and deep learning-based breast cancer detection using mammograms. *Phys Med.* 2023;114:103138. doi:10.1016/j.ejmp.2023.103138
- [11] Sahu A, Das PK, Meher S. An automatic sparse-based deep cascade framework with multilayer representation for detecting breast cancer. *Measurement.*

- 2024;228:114375. doi:10.1016/j.measurement.2024.114375
- [12] Shao W, McCollough T. Advances in microwave near-field imaging: prototypes, systems, and applications. *IEEE Microw Mag.* 2020;21(5):94–119. doi:10.1109/MMM.2020.2971375
- [13] Kranold L, Boparai J, Fortaleza L, et al. Skin phantoms for microwave breast cancer detection: a comparative study. *IEEE J Electromagn RF Microw Med Biol.* 2022;6(2):175–181. doi:10.1109/Jerm.2021.3084126
- [14] Bevacqua MT, Meo SD, Crocco L, et al. Millimeter-waves breast cancer imaging via inverse scattering techniques. *IEEE J Electromagn RF Microw Med Biol.* 2021;5(3):246–253. doi:10.1109/jerm.2021.3052096
- [15] Zhang H. Microwave imaging for breast cancer detection: the discrimination of breast lesion morphology. *IEEE Access.* 2020;8:107103–107111. doi:10.1109/access.2020.3001039
- [16] Iliopoulos I, et al. Enhancement of penetration of millimeter waves by field focusing applied to breast cancer detection. *IEEE Trans Biomed Eng.* 2021;68(3):959–966. doi:10.1109/tbme.2020.3014277
- [17] Alibakhshikenari M, et al. Metamaterial-inspired antenna array for application in microwave breast imaging systems for tumor detection. *IEEE Access.* 2020;8:174667–174678. doi:10.1109/access.2020.3025672
- [18] Nguyen DH, Stindl J, Slanina T, et al. High frequency breast imaging: experimental analysis of tissue phantoms. *IEEE Open J Antennas Propag.* 2021;2:1098–1107. doi:10.1109/ojap.2021.3127653
- [19] Sharma MK, Singh SP, Badola P, et al. Noninvasive microwave-multielement sensor for breast phantoms analysis and tumor detection. *IEEE Sens J.* 2023;23(17):20207–20214. doi:10.1109/jsen.2023.3296740
- [20] Sharma MK, Kumar M, Saini JP, et al. Experimental investigation of the breast phantom for tumor detection using ultra-wide band-MIMO antenna sensor (UMAS) probe. *IEEE Sens J.* 2020;20(12):6745–6752. doi:10.1109/jsen.2020.2977147
- [21] Porter E, Bahrami H, Santorelli A, et al. A wearable microwave antenna array for time-domain breast tumor screening. *IEEE Trans Med Imaging.* 2016;35(6):1501–1509. doi:10.1109/tmi.2016.2518489
- [22] Rajalakshmi G, Danasegaran SK, Pandian R, et al. A novel tree-slotted metamaterial terahertz antenna to diagnose breast cancer cells. *Opt Quantum Electron.* 2024;56(8):1–15. doi:10.1007/s11082-024-07220-x
- [23] Rezeg M, Hlali A, Zairi H. THz biomedical sensing for early cancer detection: metamaterial graphene biosensors with rotated split-ring resonators. *IEEE Photonics J.* 2024;16(4). doi:10.1109/jphot.2024.3413528
- [24] Singh K, Dhayal M, Dwivedi S. Breast cancer detection by terahertz UWB microstrip patch antenna loaded with 6×6 SRR array. *IETE J Res.* 2024;70(5):5295–5310. doi:10.1080/03772063.2023.2233474
- [25] Lee CS, Yang CL. Thickness and permittivity measurement in multi-layered dielectric structures using complementary split-ring resonators. *IEEE Sens J.* 2014;14(3):695–700. doi:10.1109/jsen.2013.2285918
- [26] Giuliano AE, Edge SB, Hortobagyi GN. Eighth edition of the AJCC cancer staging manual: breast cancer. *Ann Surg Oncol.* 2018;25(7):1783–1785. doi:10.1245/s10434-018-6486-6
- [27] Breast cancer: stages. Cancer.Net. [cited 2023 Dec 23]. Available from: <https://www.cancer.net/cancer-types/breast-cancer/stages>
- [28] Jesinger RA. Breast anatomy for the interventionalist. *Tech Vasc Interv Radiol.* 2014;17(1):3–9. doi:10.1053/j.tvir.2013.12.002
- [29] Martellosio A, Pasian M, Bozzi M, et al. Dielectric properties characterization from 0.5 to 50 GHz of breast cancer tissues. *IEEE Trans Microw Theory Tech.* 2017;65(3):998–1011. doi:10.1109/tmtt.2016.2631162
- [30] Dielectric properties of biological materials. In: Bioengineering and biophysical aspects of electromagnetic fields; 2018. p. 87–136. doi:10.1201/9781315221540-11
- [31] Giuliani A. The application of principal component analysis to drug discovery and biomedical data. *Drug Discov Today.* 2017;22(7):1069–1076. doi:10.1016/j.drudis.2017.01.005
- [32] Kazemi F, Mohanna F, Ahmadi-Shokouh J. Detection of biological abnormalities using a near-field microwave microscope. *Int J Microw Wirel Technol.* 2018;10(8):933–941. doi:10.1017/S1759078718000752
- [33] Bahramiabarghouei H, Porter E, Santorelli A, et al. Flexible 16 antenna array for microwave breast cancer detection. *IEEE Trans Biomed Eng.* 2015;62(10):2516–2525. doi:10.1109/tbme.2015.2434956